

Gain-Based Computing with Manifold Reduction of Soft-Spins vs Quantum Annealing in Ising Hamiltonian Minimization

James S. Cummins¹, Hayder Salman^{2,3} and Natalia G. Berloff^{1,*}

¹*Department of Applied Mathematics and Theoretical Physics,
University of Cambridge, Wilberforce Road, Cambridge CB3 0WA, United Kingdom*

²*School of Mathematics, University of East Anglia,
Norwich Research Park, Norwich, NR4 7TJ, UK,*

³*Centre for Photonics and Quantum Science, University of East Anglia,
Norwich Research Park, Norwich, NR4 7TJ, UK*

We investigate the minimization of the Ising Hamiltonians, comparing the performance of gain-based computing based on the dynamics of semi-classical soft-spin models with quantum annealing. We systematically analyze how the energy landscape for the circulant couplings of a Möbius graph evolves with increased annealing parameters. Our findings indicate that these semi-classical models face challenges due to a widening dimensionality landscape. To counteract this issue, we introduce the ‘manifold reduction’ method, which restricts the soft-spin amplitudes to a defined phase space region. Concurrently, quantum annealing demonstrates a natural capability to navigate the Ising Hamiltonian’s energy landscape due to its operation within the comprehensive Hilbert space. Our study indicates that physics-inspired or physics-enhanced optimizers will likely benefit from combining classical and quantum annealing techniques.

Pursuing enhanced computing speed and power efficiency has led to exploring alternatives to traditional electronic systems in solving complex tasks. Optical Neural Networks (ONNs) promise unprecedented parallelism, potentially superior speeds, and reduced power consumption. ONNs encode neural weights as phase shifts or changes in light intensity, with activation functions instantiated via nonlinear optical materials or components or via a strong hybridization to matter excitations [1]. They offer the potential to operate in the terahertz range, vastly surpassing the gigahertz frequencies of conventional electronic systems that can be exploited in machine learning and combinatorial optimization. The common feature of ONNs is to utilize a network of optical oscillators dynamically described by a coupled system of soft-spin models on complex-valued field $\psi_i = r_i \exp[i\theta_i]$ that has the amplitude r_i (referred to as ‘soft mode’) and phase θ_i (discrete e.g. $\theta_i = \{0, \pi\}$ or continuous ‘spin’) degrees of freedom. Each spin in the network can be associated with the quadrature of the optical complex-valued fields, thereby reducing the system to a model of real soft-spins given by $r_i \cos \theta_i$ which we analyze hereafter.

Optical parametric oscillator (OPOs) based coherent Ising machines (CIM) [2–5], lasers [6–8], spatial light modulators [9], lattices of polariton [10, 11], photon condensates [12], Microsoft analogue iterative machine [13] and Toshiba simulated bifurcation machine [14] can all minimize the classical hard-spin Ising Hamiltonians (HSIH) $H_I = -\sum_{i,j} J_{ij} s_i s_j$ with $s_i = \pm 1$ for a coupling matrix \mathbf{J} and other spin Hamiltonians (e.g. XY Hamiltonians $H_{XY} = -\sum_{i,j} J_{ij} \mathbf{s}_i \cdot \mathbf{s}_j$ with $\mathbf{s}_i = (\cos \varphi_i, \sin \varphi_i)$) using soft-spin bifurcation dynamics via the Aharonov-Hopf bifurcation [15]. This principle of operation leads to an exciting new paradigm known as “gain-based computing”. The concept behind gain-based computing is that

computational problems can be encoded in the gain and loss rates of driven-dissipative systems, which are then driven through a symmetry-breaking transition (bifurcation), selecting a mode that minimises losses. Such soft-spin models exploit enhanced dimensionality, marked by small energy barriers during amplitude bifurcation, but also complicate the energy landscape with numerous local minima. In parallel to these methods, quantum annealing is another approach to minimize the HSIH. Despite numerous studies contrasting classical and quantum methods, the limitations of currently available hardware and limitations of simulating quantum systems classically have led to contrasting conclusions as to whether a quantum advantage can potentially be realized using quantum annealing [16–23] and in particular, how quantum annealers such as D-wave perform in comparison with CIM [24]. In the latter, the connectivity of the coupling matrix was assumed to be a key factor in performance differences between these machines [24]. In Supp.Inf. section we illustrate the principle of gain-based computing and contrast it with quantum annealing and simulated bifurcation.

Using ONNs for optimization has shown promise, yet key questions remain: ‘what are suitable benchmarks for optical machines, how to guide annealing to aid optimization, what are the ONN energy landscape dynamics during annealing to ensure the optimal state is achieved, what are the distinguishing features between quantum and classical annealing?’. Answers often rely on the coupling matrix \mathbf{J} . An instructive problem should be technologically feasible, have controllable couplings, possess non-trivial structures resistant to simple local perturbations, and be mathematically tractable. Moreover, it is better to have deterministic rather than random couplings to avoid the issues of statistical convergence

[25, 26].

Here, we analyse and contrast gain-based computing (GBC) for soft-spin Ising models (SSIM) with quantum annealing for circulant coupling matrices that arise for Möbius ladder graphs, which allow complete control of frustration, energy gaps, and the structure of critical points. Furthermore, the potential to realize them in future optical systems [27] make them more suitable to consider over previously reported benchmarks [28–30]. A highlighted challenge for SSIM annealing lies in the opposing relationship between local and global minima when mapping the Ising Hamiltonian to the energy of the soft-spin system [26]. Notably, we demonstrate that quantum annealing within the whole Hilbert space of the hard-spin system navigates this challenge. Additionally, we suggest that ‘manifold reduction’, aligning amplitudes to the mean, is needed to augment the likelihood of SSIM to finding the global minima.

Möbius Ladder Graphs: Cyclic graphs with N nodes are characterized by an $N \times N$ circulant coupling matrix \mathbf{J} , constructed through cyclical permutations of any N -vector. These graphs inherently have vertex permutation symmetry, signifying boundary periodicity and uniform neighbourhoods. The structure of a circulant matrix is contained in any row, and its eigenvalues and eigenvectors can be analytically derived using the N roots of unity of a polynomial, where the row components of the matrix act as coefficients: $\lambda_n = \sum_{j=1}^N J_{1,j} \cos[\frac{2\pi n}{N}(j-1)]$ [31–35].

We consider the minimization of the Ising Hamiltonian, $H = -\frac{1}{2} \sum_{i,j=1}^{N,N} J_{ij} s_i s_j$, on a particular form of a cyclic graph – a Möbius ladder graph with even number of vertices N such that the i -th vertex has two edges connecting it to vertices $i \pm 1$ with antiferromagnetic coupling with strength $J_{i,i\pm 1} = -1$ (*circle couplings*), and an additional antiferromagnetic coupling with vertex $i + N/2$ with strength $J_{i,i+N/2} = -J, J > 0$ (*cross-circle couplings*). We denote by S_0 the state where the spins, s_i , alternate along the ring so that $s_i s_{i\pm 1} = -1$ for all i (Fig. 1(a)), and by S_1 the state where the spins alternate everywhere except at two positions on the opposite sides of the ring: $s_i s_{i+1} = -1$ for all $i \neq i_0$ and $s_{i_0} s_{i_0+1} = s_{i_0+N/2} s_{i_0-1+N/2} = 1$ Fig. 1(b)). When $N/2$ is odd, S_0 is always the ground state with energy $H_1(J) = -(J+2)N/2$. When $N/2$ is even, the S_0 configuration has Hamiltonian $H_1^{(0)}(J) = (J-2)N/2$ and S_1 has $H_1^{(1)}(J) = 4 - (J+2)N/2$. Therefore, S_0 [S_1] is the global minimum (while S_1 [S_0] is the excited state) if $J < J_{\text{crit}} \equiv 4/N$ [$J > J_{\text{crit}}$]. The eigenvalues of the coupling matrix \mathbf{J} for the Möbius ladder with $J_{1,j} \in \{-1, 0, -J\}$ are $\lambda_n = -2\cos(2\pi n/N) - J(-1)^n$. Equating the two largest eigenvalues $2\cos(2\pi/N) + J$ and $2 - J$ gives the value of $J = J_e = 1 - \cos(2\pi/N)$ at which the leading eigenvectors change. When $J_e < J < J_{\text{crit}}$ the eigenvalues for S_0 are less than that for S_1 despite

S_0 being the lower energy state (see Supp. Inf. for the detailed derivation of the spectra). This is in contrast to computationally simple problem instances, in which the ground state minimizer is located at the hypercube corner of the projected eigenvector corresponding to the largest eigenvalue [36].

Soft Spin Ising Model (SSIM): The ONNs based on laser operation are non-Hermitian systems that tend to minimise losses on their route to coherence. The losses can be written as an ‘energy’ (‘cost’) function to be minimized. For instance, CIM’s energy landscape to be minimised (in a classical limit) is

$$E = \frac{C}{4} \sum_{i=1}^N (p(t) - x_i^2)^2 - \frac{1}{2} \sum_{i=1}^N \sum_{j=1}^N J_{ij} x_i x_j, \quad (1)$$

where x_i are quadratures of the OPOs, $p(t)$ describes the effective laser pumping power (injection minus linear losses), and C corresponds to the strength of saturable nonlinearity. As $p(t)$ grows from a large negative to large positive $p(t) = p_\infty$ values, E anneals from the dominant convex first term on the right-hand side of Eq. (1) that is minimized at $x_i = 0$ for all i to the minimum of the second term which is the scaled target Ising Hamiltonian with $x_i = \pm \sqrt{p_\infty}$. The temporal change of $p(t)$, therefore, is the annealing parameter combined with a gradient descent as

$$\dot{x}_i = -\frac{\partial E}{\partial x_i} = C(p(t)x_i - x_i^3) + \sum_{i \neq j} J_{ij} x_j. \quad (2)$$

All ONN soft spin optimizers exploit this central principle, while the details of the nonlinearity or the gradient dynamics can vary from platform to platform [15]. In particular, CIM dynamics is an example of the Hopfield-Tank network (HT) $\dot{x}_i = p(t)x_i + \sum_{i \neq j} J_{ij} x_j$ also used [37] for Ising Hamiltonian minimization [38]. Another approach uses the second-order resonance to project the XY onto the Ising dynamics [39].

Eq. (1) has real amplitudes x_i . As the laser pumping $p(t)$ increases from negative values, the minimizers \mathbf{x}^* of Eq. (1) and minima of E change. We associate Ising spins with x_i via $s_i = x_i/|x_i|$. We expect that the soft-spin energy state E_0 that corresponds to the hard-spin Ising state S_0 and depicted in Fig. (1)(a) is symmetric in amplitudes as all spins experience the same frustration of the cross-circle coupling, so all amplitudes have the same modulus $|x_i| = X$. From Eq. (2) X satisfies $X = \sqrt{p(t) + (2-J)/C}$ with the corresponding soft-spin energy $E_0 = (J-2)N(2-J+2Cp)/4$. This state can be realised from a vacuum state when $p(t)$ exceeds $(J-2)/C$.

The soft-spin energy state E_1 corresponding to S_1 , when two side edges are frustrated, is asymmetric in amplitudes. This asymmetry is shown schematically in Figs. (1)(b,c). This occurs because the lower energy is achieved if the amplitudes connected by the frustrated

edges $|x_i| = X_L$ are lower than in the rest of the system. For $N = 8$ in Fig. (1)(b), there are two types of amplitudes: 4 nodes with $\pm|X_L|$ and 4 with amplitudes $|x_i| = X_B$, where $X_B = (1 - J - Cp)X_L + CX_L^3$ as obtained from the steady states of Eq. (2) governing the dynamics of X_L , while the steady-state on the evolution of X_L gives $(p + 1 + J)X_B + X_L = X_B^3$. These are in agreement with the dynamical simulations presented in Figs. (2)(b). By solving the polynomial equation for X_L , we can compute E_1 across any p, J, N , and C . This allows us to discern regions in this parameter space where the global minimum aligns with either E_0 or E_1 and confirm if these states correspond with the hard-spin Ising Hamiltonian's global minimum. Figure (1)(d) depicts distinct regions in the $J - p$ parameter space. Within the $J_e < J < J_{\text{crit}}$ interval S_0 emerges as the hard-spin Ising model's lowest energy state. For the soft-spin model, however, only the region shown in pink corresponds to this state (E_0). Figure (1)(d) shows that for values $J_e < J < J_{\text{crit}}$, as laser power p rises, the E_0 state becomes the energy minimum for the soft-spin model, aligning with the hard-spin Ising Hamiltonian's S_0 . Yet, the success probability of converging to the true ground state does not increase beyond 0.2 as shown in Fig.(1)(e). This is a consequence of increasing amplitudes that bring the increased height of the energy barriers that prevent the system from transitioning to the state, S_0 (see Fig. (1)(f)). Figure 3 in Supp.Inf. provides further context, depicting basins of attraction for a diverse set of values, p , within a fixed range $J_e < J < J_{\text{crit}}$. The space structure of soft spin models can be further understood by considering the critical points of their energy landscape for different annealing parameter values [40]; (see Supp. Inf).

Manifold Reduction for SSIM: These considerations suggest that amplitude heterogeneities have a severely detrimental effect on the optimization process in some regions of parameter space as they allow the soft-spin energy landscape to find and follow its ground state, which is quite different from the ground state of the hard-spin Ising Hamiltonian. This problem has been recognised before [41, 42], but in the context of the final state, so various feedback schemes were suggested to bring all amplitudes to the same value, say, ± 1 at the end of the simulations. This could be achieved, for instance, by changing the laser intensity individually for each spin as $\dot{p}_i(t) = \epsilon(1 - x_i^2)$, where ϵ is a small constant parameter. However, as our results on the simple circulant graphs illustrate, this feedback does not change the most essential part of the dynamics during the pitchfork bifurcation from the vacuum state. Moreover, this feedback becomes important only for amplitudes sufficiently close to ± 1 when the barriers between states are already too high.

To circumvent this behaviour, we introduce feedback restricting the soft spin energy landscape to keep them close to the average value. This restriction can be

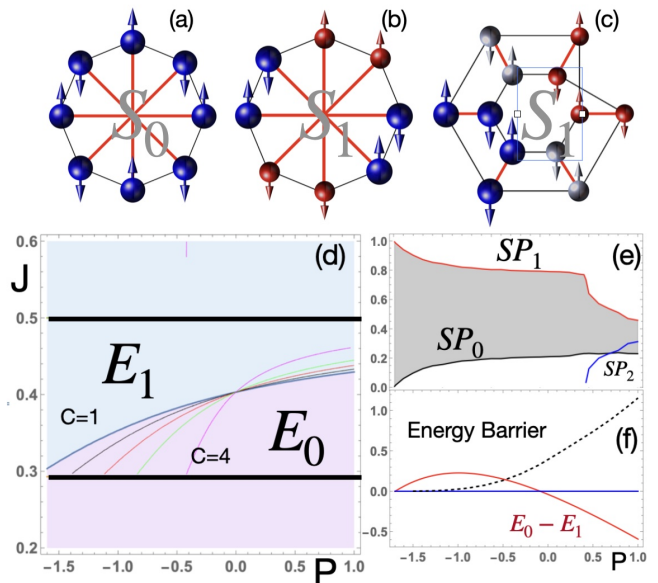


Figure 1. (a-c) Schematic representation of the states realised by soft-spin models of Eq. (1) on the Möbius ladder graphs with varying cross-ring couplings (shown in red). (a),(b) and (c) depict states that map onto S_0 , S_1 Ising states for $N = 8$ and S_1 state for $N = 12$, respectively. (c) uses a different node arrangement that illustrates the graph relationship with the topology of the Möbius strip. The same colours are used to show equal intensities; the larger sizes correspond to larger intensities. (d) Regions of different global minima of Eq. (1): E_1 in the blue region and E_0 in the pink region, in $J - p$ space for $N = 8, C = 1$. Two critical values of J are shown as solid black lines. Between these lines, S_0 is expected as the hard-spin Ising model global minimizer. Thin lines show the contours $E_1 = E_0$ for $C = 1, 1.2, 1.5, 2, 4$ in that region. (e) Success probability of reaching E_0 (labelled as SP_0) and E_1 (labelled as SP_1) states of the soft-spin energy in Eq. (1) from a point \mathbf{x} with randomly chosen components x_i in $[-1, 1]$ for different values of p and $J = 0.4, N = 8, C = 1$. For larger values of p a third state of higher energy appears with the success probability SP_2 ; when projected on spins $s_i = x_i/|x_i|$ this state corresponds to S_1 . (f) The height of the minimum energy barrier between E_1 and E_0 calculated as the energy difference between E_1 and energy of the nearest saddle point is shown as a black dashed line for $J = 0.4, C = 1$. The difference between E_0 and E_1 is shown in red.

achieved by modifying the signal intensities bringing them towards the average mass per particle defined by the squared radius of the quadrature $R(\mathbf{x}) \equiv \sum_{i=1} x_i^2/N$

$$x_i \rightarrow (1 - \delta)x_i + \delta R x_i / |x_i|. \quad (3)$$

If $\delta = 0$, then no adjustment is made. If $\delta = 1$, then all amplitudes are set to the same (average) value. For $0 < \delta < 1$, $1/\delta$ determines the proportion of the effective space for the restricted evolution.

Figure (2)e shows the probability of finding the ground state of the Ising Hamiltonian using the HT networks [37], Eq.(2) (CIM-I), Eq.(2) with individual pumping adjustments $p \rightarrow p_i$ according to $\dot{p}_i = \epsilon(1 - x_i^2)$ (CIM-II), and

Eq.(2) with manifold reduction by Eq. (3) (CIM-III). For CIM-I and CIM-III, we set $p(t) = (1 - p_0) \tanh(\epsilon t) + p_0$. CIM-III shows a significant improvement in finding the ground state compared with other models. Thus, in soft-spin models, the imperative to constrain the manifold implies that dimensional annealing should be tailored according to the energy landscape's characteristics [40]. Next, we study the quantum evolution on the Ising energy landscape of circulant coupling matrices to contrast its performance with the soft-spin nonlinear models.

Quantum Annealing: We consider the transverse field Ising model given by

$$\hat{H} = -\frac{1}{2} \sum_{\substack{i,j=1 \\ i \neq j}}^{N,N} J_{ij} \hat{S}_i^z \hat{S}_j^z - \sum_{i=1}^N h_i \hat{S}_i^z - \gamma(t) \sum_{i=1}^N \hat{S}_i^x, \quad (4)$$

where \hat{S}^α are the spin-1/2 Pauli matrices (see Supp. Inf.). The first term, \hat{H}_0 , is diagonal and represents the classical Ising Hamiltonian H_I ; the second term is a symmetry-breaking longitudinal magnetic field; the third term is a transverse field that results in a non-diagonal Hamiltonian operator and gives rise to the quantum Ising model. We will take the annealing term to be of the form $\gamma(t) = B/\sqrt{t+t_0}$ for some constant B [43] and set $t_0 = 0.5$.

We begin with an initial state, which is the ground state of the transverse field Hamiltonian. The initial state at time t_i can then be expressed as $|\Psi(t_i)\rangle = |\psi_{\rightarrow}\rangle \otimes \dots \otimes |\psi_{\rightarrow}\rangle$ where for each subsystem $|\psi_{\rightarrow}\rangle = (|\uparrow\rangle + |\downarrow\rangle)/\sqrt{2}$. The wavefunction is then evolved according to the time-dependent Schrödinger equation (see Supp. Inf. for details) [44]. As $t \rightarrow \infty$, $\gamma(t) \rightarrow 0$ and the contribution of the last term decays to bring about the target Hamiltonian. Provided $\gamma(t)$ is varied adiabatically, the system evolves, remaining in the true ground state of the system, and settles into the target Hamiltonian's desired ground state at sufficiently long times.

To determine the probability of finding the ground state, we compute the projection of $|\Psi(t)\rangle$ onto the ground state $|\phi_{\text{GS}}\rangle$ of the classical Hamiltonian, \hat{H}_0 , given by $P_{\text{GS}} = |\langle \phi_{\text{GS}} | \Psi(t) \rangle|^2$. For $J < J_{\text{crit}}$, the S_0 ground state has a two-fold degeneracy. Therefore, we can expect that the probability of finding one of the ground states is $P_{\text{GS}} = 1/2$. In Fig. 2f, we present numerical simulations of the time evolution of the success probability for finding the ground state of $N = 8$ spin system for $J = 0.35$. For comparison, we have also included the results for simulated annealing [45] and classical annealing by evolving a master equation [43] (see Supp. Inf. for details). In the former, we allow transition probabilities for single-spin flips only, whereas, in the latter, we allow for all spin flips to reveal the importance of spin correlations on the success probability of finding the ground states. As can be seen from Fig. 2f, for the chosen annealing schedule, only simulated annealing does not converge to the

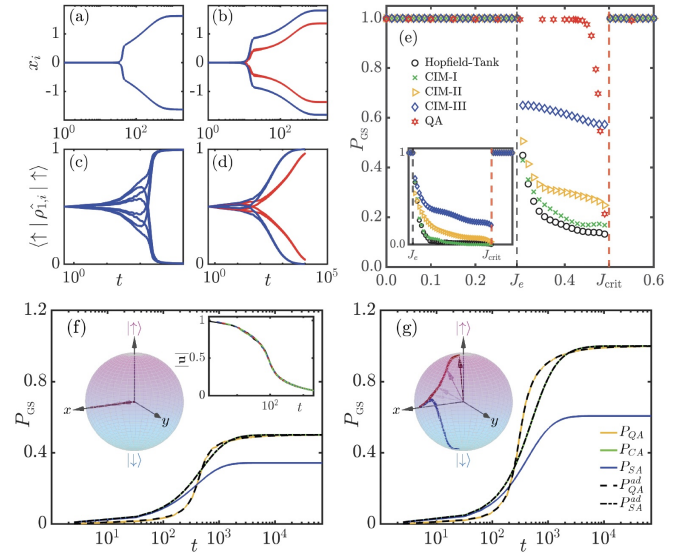


Figure 2. (a) Evolution of $N = 8$ soft spins for $J = 0.35$ and (b) $J = 0.55$ according to Eq. (2). In each case, the ground state is recovered. The amplitudes connected by the frustrated edges are lower than in the rest of the system and are shown in red. In all runs, $C = 1$, $p_0 = J - 2$, $\epsilon = 0.003$, $\Delta t = 0.1$, and each $x_i(0)$ is chosen randomly from a uniform distribution in the range $[-0.001, 0.001]$; (c) Similar evolution for probability amplitude of $|\uparrow\rangle$ state in quantum annealing simulation for $h_i = 0.05|\xi\rangle_{S_0} + 0.005|\xi\rangle_{S_1}$ with $J = 0.35$ and (d) $J = 0.6$. The amplitudes colored in red correspond to the frustrated spins as in (b); (e) Ground state probability for HT, CIM-I, CIM-II, CIM-III, and quantum annealing (QA) for the Möbius ladder graph with $N = 8$. For CIM-III, for each value of J , the optimum value of $0 < \delta < 1$ is chosen based on a set of preliminary runs in which δ is varied. Two thousand runs are used to calculate the probability of finding the ground state P_{GS} for each value of J . For QA, $B = 5$ and $\Delta t = 0.1$. Inset to (e) shows the same plots but for $N = 100$; (f) Ground state probability of target Hamiltonian with $J = 0.35$ and $B = 5$ for quantum annealing (QA), single-spin simulated annealing (SA), classical annealing (CA) and corresponding probabilities expected for adiabatic simulated (SA-ad) and adiabatic quantum (QA-ad) annealing. Insets show Bloch vector for single-spin and magnitude of Bloch vector $|\mathbf{u}|$; (g) similar results as (f) but with symmetry-breaking terms of the form $h_i = 0.05|\xi\rangle_{S_0} + 0.05|\xi\rangle_{S_1}$ added to Hamiltonian; Bloch sphere shows typical trajectories of two neighbouring spins.

correct ground states of the system. In contrast, quantum and classical annealing recover the correct ground states even though our value of J lies within the range $J_e < J < J_{\text{crit}}$. Although the convergence of SA can be enhanced with different annealing schedules, in general, the success probabilities are lower than the other algorithms we have investigated over a range of annealing schedules (see Supp. Inf. and Ref. [43]).

To compare the quantum annealing and semi-classical soft-spin simulations, we computed the single-spin reduced density matrix $\hat{\rho}_{1,i}$ from the pure state $|\Psi(t)\rangle$. In general, the single-spin density matrix will correspond to

entangled states. This is illustrated by recovering the Bloch vector from $\hat{\rho}_{1,i}(t)$ (see Supp. Inf. for details). In the inset of Fig. (2)f, we show the evolution of the Bloch vector with time for one of the spins (other spins show similar behaviour). We see that the spin is initially aligned along the equator (consistent with the form of $|\psi_{\rightarrow}\rangle$) but shrinks towards the origin as the state evolves. The departure of the Bloch vector from the surface of the Bloch sphere is indicative of quantum entanglement while its dynamics towards the origin signals a spin state that is maximally entangled with the rest of the system. A definite state emerges only upon measurement, which then subsequently collapses the corresponding wavefunction to one specific configuration.

For direct comparison with the deterministic semi-classical simulations, we removed the ground state degeneracy in our quantum annealing simulations by introducing the symmetry-breaking term \hat{H}_1 in Eq.(4). We set h_i to correspond to $0.05|\xi\rangle_{S_0} + 0.05|\xi\rangle_{S_1}$ where $|\xi\rangle_{S_0}$ and $|\xi\rangle_{S_1}$ correspond to the S_0 or S_1 state, respectively. This enforces the evolution towards a specific ground state without the final state being in a quantum superposition. The resulting Bloch vector for $J = 0.35$ is shown in the inset of Fig. 2g and now indicates evolution that ends at the surface of the Bloch sphere, reaching either the $|\uparrow\rangle$ or $|\downarrow\rangle$ state. This evolution clearly demonstrates that though individual spins converge towards a non-correlated value, their evolution bears the imprint of inter-spin correlations. Unlike the semi-classical models, our quantum annealing algorithm consistently identifies the correct ground state in the $J_e < J < J_{\text{crit}}$ range; (see Fig. 2e) and demonstrates that correlations play a key role in facilitating the system to converge to the true ground state. However, its performance appears to degrade near J_{crit} . In contrast, the gain-based algorithm based on the CIM is less sensitive near J_{crit} and indicates one of the potential advantages of gain-based algorithms.

The corresponding time-dependent probability of finding each spin, i , in the $|\uparrow\rangle$ state is presented in Fig. 2c for $J = 0.35$ (and for $J = 0.6$ in Fig. 2d). We see that even though we have strongly perturbed the system towards the S_1 state for $J = 0.35$, the results emphasize the quantum annealing algorithm's capacity to find the correct ground state during gradual $\gamma(t)$ quenches, leveraging the quantum system's expanded phase space.

In summary, we analysed the optimization of Ising Hamiltonians, contrasting the classical dynamics of semi-classical soft-spin models with quantum annealing. We discussed the challenges for semi-classical models due to a broadening dimensionality landscape, especially when the models' global minimum maps to the Ising Hamiltonian's excited state. A solution, termed 'manifold reduction', is presented, constraining the soft-spin amplitudes and restricting the dimensionality landscape. On the other hand, we showed that quantum annealing inherently can traverse the Ising Hamiltonian's energy ter-

rain but is more sensitive near quantum critical points. The findings highlight the importance of understanding the influence of dimensionality and the energy landscape overall on optimising physical systems. Furthermore, they demonstrate how extensions of semi-classical models to include quantum effects has the potential to assist the annealing in navigating the system towards the true ground state by leveraging the advantages of both gain-based and quantum algorithms.

ACKNOWLEDGEMENTS

J.S.C. acknowledges the PhD support from the EPSRC, N.G.B acknowledges the support from HORIZON EUROPE/UKRI CL4-2021-DIGITAL-02-16, and Weizmann-UK Make Connection grant 142568.

* correspondence address: N.G.Berloff@damtp.cam.ac.uk

- [1] J. Kasprzak, M. Richard, S. Kundermann, A. Baas, P. Jeambrun, J. Keeling, F. Marchetti, M. Szymańska, R. André, J. Staehli, *et al.*, *Nature* **443**, 409 (2006).
- [2] Y. Yamamoto, K. Aihara, T. Leleu, K.-i. Kawarabayashi, S. Kako, M. Fejer, K. Inoue, and H. Takesue, *npj Quantum Information* **3**, 1 (2017).
- [3] T. Inagaki, Y. Haribara, K. Igarashi, T. Sonobe, S. Tamate, T. Honjo, A. Marandi, P. L. McMahon, T. Umeki, K. Enbutsu, *et al.*, *Science* **354**, 603 (2016).
- [4] P. L. McMahon, A. Marandi, Y. Haribara, R. Hamerly, C. Langrock, S. Tamate, T. Inagaki, H. Takesue, S. Utsunomiya, K. Aihara, *et al.*, *Science* **354**, 614 (2016).
- [5] T. Honjo, T. Sonobe, K. Inaba, T. Inagaki, T. Ikuta, Y. Yamada, T. Kazama, K. Enbutsu, T. Umeki, R. Kasahara, K. ichi Kawarabayashi, and H. Takesue, *Science Advances* **7**, eabh0952 (2021), <https://www.science.org/doi/pdf/10.1126/sciadv.abh0952>.
- [6] V. Pal, S. Mahler, C. Tradonsky, A. A. Friesem, and N. Davidson, *Physical Review Research* **2**, 033008 (2020).
- [7] M. Babaeian, D. T. Nguyen, V. Demir, M. Akbulut, P.-A. Blanche, Y. Kaneda, S. Guha, M. A. Neifeld, and N. Peyghambarian, *Nature communications* **10**, 1 (2019).
- [8] M. Parto, W. Hayenga, A. Marandi, D. N. Christodoulides, and M. Khajavikhan, *Nature materials* **19**, 725 (2020).
- [9] D. Pierangeli, G. Marcucci, and C. Conti, *Physical review letters* **122**, 213902 (2019).
- [10] N. G. Berloff, M. Silva, K. Kalinin, A. Askitopoulos, J. D. Töpfer, P. Cilibrizzi, W. Langbein, and P. G. Lagoudakis, *Nature materials* (2017).
- [11] K. P. Kalinin, A. Amo, J. Bloch, and N. G. Berloff, *Nanophotonics* **9**, 4127 (2020).
- [12] M. Vretnar, B. Kassenberg, S. Bissesar, C. Toebes, and J. Klaers, *Physical Review Research* **3**, 023167 (2021).
- [13] K. Kalinin, G. Mourgiaris-Alexandris, H. Ballani, N. G. Berloff, J. H. Clegg, D. Cletheroe, C. Gkantsidis, I. Haller, V. Lyutsarev, F. Parmigiani, L. Pickup, *et al.*, arXiv preprint arXiv:2304.12594 (2023).

- [14] H. Goto, K. Endo, M. Suzuki, Y. Sakai, T. Kanao, Y. Hamakawa, R. Hidaka, M. Yamasaki, and K. Tatumura, *Science Advances* **7**, eabe7953 (2021).
- [15] M. Syed and N. G. Berloff, “Physics-enhanced bifurcation optimisers: All you need is a canonical complex network,” (2022).
- [16] C.-W. Liu, A. Polkovnikov, and A. W. Sandvik, *Phys. Rev. Lett.* **114**, 147203 (2015).
- [17] A. D. King, S. Suzuki, J. Raymond, A. Zucca, T. Lanting, F. Altomare, A. J. Berkley, S. Ejtemaee, E. Hoskinson, S. Huang, E. Ladizinsky, A. J. R. MacDonald, G. Marsden, T. Oh, G. Poulin-Lamarre, M. Reis, C. Rich, Y. Sato, J. D. Whittaker, J. Yao, R. Harris, D. A. Lidar, H. Nishimori, and M. H. Amin, *Nature Physics* **18**, 1324 (2022).
- [18] B. Heim, T. F. Rønnow, S. V. Isakov, and M. Troyer, *Science* **348**, 215 (2015), <https://www.science.org/doi/pdf/10.1126/science.aaa4170>.
- [19] A. D. King, J. Raymond, T. Lanting, R. Harris, A. Zucca, F. Altomare, A. J. Berkley, K. Boothby, S. Ejtemaee, C. Enderud, E. Hoskinson, S. Huang, E. Ladizinsky, A. J. R. MacDonald, G. Marsden, R. Molavi, T. Oh, G. Poulin-Lamarre, M. Reis, C. Rich, Y. Sato, N. Tsai, M. Volkmann, J. D. Whittaker, J. Yao, A. W. Sandvik, and M. H. Amin, *Nature* **617**, 61 (2023).
- [20] T. Albash and D. A. Lidar, *Phys. Rev. X* **8**, 031016 (2018).
- [21] B. Yan and N. A. Sinitsyn, *Nature Communications* **13**, 2212 (2022).
- [22] T. Albash and D. A. Lidar, *Phys. Rev. X* **8**, 031016 (2018).
- [23] S. Muthukrishnan, T. Albash, and D. A. Lidar, *Phys. Rev. X* **6**, 031010 (2016).
- [24] R. Hamerly, T. Inagaki, P. L. McMahon, D. Venturelli, A. Marandi, T. Onodera, E. Ng, C. Langrock, K. Inaba, T. Honjo, K. Enbutsu, T. Umeki, R. Kasahara, S. Utsunomiya, S. Kako, K. Ichi Kawarabayashi, R. L. Byer, M. M. Fejer, H. Mabuchi, D. Englund, E. Rieffel, H. Takesue, and Y. Yamamoto, *Science Advances* **5**, eaau0823 (2019), <https://www.science.org/doi/pdf/10.1126/sciadv.aau0823>.
- [25] H. Ohadi, R. Gregory, T. Freearde, Y. Rubo, A. Kavokin, N. Berloff, and P. Lagoudakis, *Physical Review X* **6**, 031032 (2016).
- [26] B. P. Marsh, R. M. Kroeze, S. Ganguli, S. Gopalakrishnan, J. Keeling, and B. L. Lev, “Entanglement and replica symmetry breaking in a driven-dissipative quantum spin glass,” (2023), [arXiv:2307.10176 \[quant-ph\]](https://arxiv.org/abs/2307.10176).
- [27] M. Calvanese Strinati, D. Pierangeli, and C. Conti, *Phys. Rev. Appl.* **16**, 054022 (2021).
- [28] F. Hamze, J. Raymond, C. A. Pattison, K. Biswas, and H. G. Katzgraber, *Physical Review E* **101**, 052102 (2020).
- [29] D. Roberts, L. Cincio, A. Saxena, A. Petukhov, and S. Knysh, *Physical Review A* **101**, 042317 (2020).
- [30] S. Mandrà, G. Mossi, and E. G. Rieffel, *arXiv preprint arXiv:2308.09704* (2023).
- [31] D. Kalman and J. E. White, *The American Mathematical Monthly* **108**, 821 (2001).
- [32] H. Zhang and Y. Yang, *International journal of quantum chemistry* **107**, 330 (2007).
- [33] J. Gancio and N. Rubido, *Chaos, Solitons & Fractals* **158**, 112001 (2022).
- [34] A. B. Ayoub and D. Psaltis, *Scientific Reports* **11**, 1 (2021).
- [35] X. Qiang, T. Loke, A. Montanaro, K. Aungskunsiri, X. Zhou, J. L. O’Brien, J. B. Wang, and J. C. Matthews, *Nature communications* **7**, 1 (2016).
- [36] K. P. Kalinin and N. G. Berloff, *arXiv preprint arXiv:2008.00466* (2020).
- [37] J. J. Hopfield, *Proceedings of the national academy of sciences* **79**, 2554 (1982).
- [38] J. J. Hopfield and D. W. Tank, *Biological cybernetics* **52**, 141 (1985).
- [39] K. P. Kalinin and N. G. Berloff, *arXiv preprint arXiv:1806.11457* (2018).
- [40] A. Yamamura, H. Mabuchi, and S. Ganguli, “Geometric landscape annealing as an optimization principle underlying the coherent ising machine,” (2023), [arXiv:2309.08119 \[cond-mat.dis-nn\]](https://arxiv.org/abs/2309.08119).
- [41] K. P. Kalinin and N. G. Berloff, *New Journal of Physics* **20**, 113023 (2018).
- [42] T. Leleu, F. Khoystatee, T. Levi, R. Hamerly, T. Kohno, and K. Aihara, *arXiv e-prints*, *arXiv* (2020).
- [43] T. Kadowaki and H. Nishimori, *Phys. Rev. E* **58**, 5355 (1998).
- [44] A. Norambuena, D. Tancara, and R. Coto, *European Journal of Physics* **41**, 045404 (2020).
- [45] S. Kirkpatrick, C. D. Gelatt, and M. P. Vecchi, *Science* **220**, 671 (1983), <https://www.science.org/doi/pdf/10.1126/science.220.4598.671>.